

The Plasmon modes of graphene nanoribbons with periodic planar arrangements

C. Vacacela Gomez^{†,‡}, M. Pisarra^{§,‡}, M. Gravina^{†,‡}, J. M. Pitarke^{○,¶}, and A. Sindona^{†,‡,*}

[†]*Dipartimento di Fisica, Università della Calabria, Via P. Bucci, Cubo 30C, I-87036 Rende (CS), Italy*

[‡]*INFN-LNF, Gruppo collegato di Cosenza, Via P. Bucci, Cubo 31C, I-87036 Rende (CS), Italy*

[§]*Departamento de Química, Universidad Autónoma de Madrid, Calle Francisco Tomás y Valiente 7 (Módulo 13), E-28049, Madrid, Spain*

[○]*CIC nanoGUNE, Tolosa Hiribidea 76, E-20018 Donostia - San Sebastian, Basque Country, Spain*

[¶]*Materia Kondentsatuaren Fisika Saila, DIPC, and Centro Fisica Materiales CSIC-UPV/EHU, 644 Posta Kutxatila, E-48080 Bilbo, Basque Country, Spain*

Abstract: The dielectric properties of narrow-width graphene nanoribbons, organized in periodic planar arrays with zigzag and armchair shaped edges, are theoretically investigated in the framework of time dependent density functional theory. Both intrinsic (undoped) and extrinsic (doped, gated) systems are scrutinized within the random phase approximation. The appearance of collective charge-density oscillations, e.g., plasmons, is discussed over a wide range of energies (from the lower terahertz to extreme ultraviolet) and momenta. Visible to ultraviolet interband excitations typical of carbon based materials (namely, the π and σ - π plasmons) are shown to exhibit high sensitivity to the ribbon chirality and width, which ends up in multiple energy-momentum dispersion branches. At the visible to infrared end of the spectrum, *unprecedented* plasmon modes of different nature are detected. In particular, semimetallic nanoribbons are observed to display an intraband plasmon that follows the typical energy-momentum dispersion of a two-dimensional electron gas. As opposite to graphene, the intensity of this mode is large relative to the high-energy excitations even at zero doping. On the other hand, semiconducting nanoribbons are found to be characterized by two distinct intraband and interband plasmons, whose interplay is extremely responsive to injection of charge carriers (electron or holes) or increase in electronic temperature. These oscillations seem to be consistent with recent nano-infrared imaging of confined edge and surface plasmon modes inside patterned graphene nanoribbons fabricated on aluminum oxide substrates.

keywords: *graphene, graphene nanoribbon, plasmonics, time dependent density functional theory*

*Supporting Information

The design of nanocarbon architectures is expected to have large impact in plasmonic technologies based around circuit elements, interconnects, antennas, waveguides, modulators and attenuators that may operate from MW up to IR frequencies¹⁻⁶. Potential applications are also envisaged in sensing, optical signal processing and quantum information technology, just to name a few. The main reason for this huge surge in interest stems from the unique electronic, optical and mechanical properties of monolayer graphene (MG) and its derivatives⁷, which can support coherent charge-density fluctuations, e.g., plasmons, when exposed to photon or electron currents⁸⁻¹². Such collective modes at THz frequencies are characterized by strong confinement, large tunability and low losses¹³ as compared to conventional plasmonic materials (e.g., gold and silver). Recent experimental achievements have allowed to launch, control, manipulate and detect plasmons in a variety of graphene related materials and heterostructures. This suggests that graphene-based plasmonic devices may become a reality soon, with the potential to operate on the ‘THz gap’, forbidden by either classical electronics or photonics^{4,14,15}.

The presence of plasmons in graphene nanoribbons (GNRs) from the nano to micro range in width has been observed over the recent years^{8,10,16,17}. On the

theoretical side, accurate density functional and tight-binding (TB) approaches have explored the electronic structure of zigzag and armchair GNRs, with particular attention to the band gap values of the intrinsic systems¹⁸⁻²². A few studies have also investigated the role of plasmon resonances in GNRs using either a semiclassical electromagnetic approach²³ or a TB scheme²⁴, and limiting the analysis to THz frequencies. Nevertheless, a comprehensive characterization of the dielectric properties of such systems is still lacking.

In this letter, we provide an ab initio study of the presence and properties of plasmon excitations in regular planar arrays of GNRs over a wide range of frequencies (from the lower THz to extreme UV) and momenta (below $\sim 0.8 \text{ \AA}^{-1}$). We use time dependent (TD) density functional theory (DFT) in the random phase approximation (RPA) and specialize to the 4ZGNR and 5AGNR geometries reported in Fig. 1(a,c). These are respectively characterized by 4 zigzag chains (Fig. 1(a)) and 5 dimer lines (Fig. 1(c)) across the GNR width¹⁸. The dangling bonds of each GNR array are passivated by hydrogen atoms on both sides. The basic parameters of the unit cells of the GNRs are fixed to their *nominal* values with a C-C bond-length of 1.42 Å and a C-H bond-length of 1.09 Å. These turn out to differ by less than 1%

from the corresponding lengths obtained by geometry optimization (Fig. S1). The unit cells are then periodically repeated along and perpendicular to the GNR axis, forming regular arrays separated by an in-plane vacuum width of 15 Å (Fig. 1(a,c)). The equilibrium electronic structures of the systems (Supporting Information, Sec. I) are computed using the local density approximation (LDA²⁵) with suitable norm-conserving pseudo-potentials²⁶ and the Plane-Wave (PW) basis²⁷. Ground state calculations are carried out on a $60 \times 1 \times 1$ Monkhorst-Pack (MP) grid²⁸, resulting in a uniform sampling of the irreducible part of the 1st BZ, i.e., the ΓX segment shown in Fig. 1(b,d). The converged electron densities are then used to calculate the Kohn-Sham (KS) eigensystems on a denser MP mesh of 180 points including up to 120 bands, which allows an accurate representation of the dielectric properties of the GNRs on the eV scale. To better explore the IR region, a more finely resolved MP sampling of 1000 points is considered with roughly 30 bands. A correct insight into the lower THz region requires an MP sampling of 12500 points, which is done by taking into account only the valence band (VB) and conduction band (CB) of the systems. The three-dimensional periodicity required by our PW-DFT approach is generated by replicating the GNR arrays over an out-of-plane distance L of 15 Å, which ensures negligible overlap (but not negligible interaction) of charge density between the replicas.

As for the LDA calculations, the different geometry of the assemblies (Fig. 1(a,c)) produces electronically distinct band dispersions and densities of states (DOS). 4ZGNR (Fig. 1(b)) appears as a semimetallic compound with the VB and CB overlapping close to the X -point. The quasi-flat dispersions near the intrinsic Fermi level E_F give rise to strong peaks in the DOS, as opposite to MG where the linear dispersing VB and CB yield a vanishing DOS at E_F . 5AGNR (Fig. 1(d)) is a semiconductor with the VB and CB having parabolic-like dispersions around a small gap of ~ 0.36 eV that result in two peaks in the DOS.

It should be noted that local spin density calculations suggest the opening of a band gap larger than 0.1 eV in ZGNRs^{18–20}. Additionally, GW approaches predict larger band gaps in both ZGNRs and AGNRs by roughly 1 eV with respect to local density calculations¹⁹. Nonetheless, band gap values of the same order of the LDA band gap of 5AGNR have been measured for some GNRs as wide as about 20 nm grown on Au(111)²². Thus, the application of an RPA scheme to the LDA band structure of 5AGNR can be of help in the interpretation of plasmon measurements on currently synthesized GNR structures¹⁷. Complementarily, the LDA analysis of a virtually gapless GNR, i.e., 4ZGNR, is particularly instructive in order to emphasize the different role played by doping.

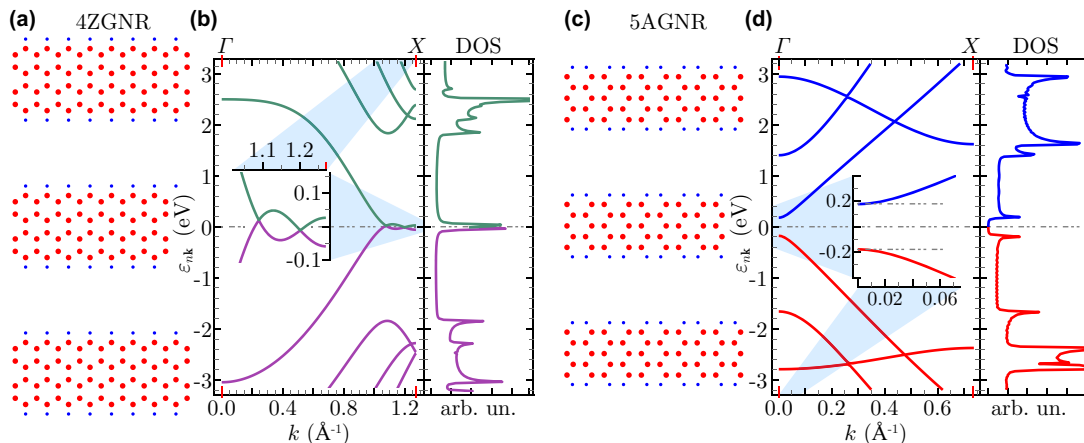


Figure 1. Geometry (a,c), electronic structure and DOS (b,d) for 4ZGNR (a,b) and 5AGNR (c,d). The insets in (b,d) zoom on the band levels around the intrinsic Fermi level, which is set to zero.

Our starting point is the density response function of *non-interacting* electrons in the GNRs, as given by the Adler-Wiser formula^{29,30}

$$\chi_{\mathbf{G}\mathbf{G}'}^0 = \frac{2}{\Omega} \sum_{\mathbf{k}, \nu, \nu'} \frac{(f_{\nu\mathbf{k}} - f_{\nu'\mathbf{k}+\mathbf{q}}) \rho_{\nu\nu'}^{\mathbf{k}\mathbf{q}}(\mathbf{G}) \rho_{\nu\nu'}^{\mathbf{k}\mathbf{q}}(\mathbf{G}')^*}{\omega + \varepsilon_{\nu\mathbf{k}} - \varepsilon_{\nu'\mathbf{k}+\mathbf{q}} + i\eta}, \quad (1)$$

which is a corollary of the Kubo formula for periodic systems³¹. Hartree atomic units are used throughout this work, unless otherwise stated. In Eq. (1) the electron

energies $\varepsilon_{\nu\mathbf{k}}$ and states $|\nu\mathbf{k}\rangle$ are indexed by the band number ν and the quasi-wavevector \mathbf{k} along the GNR axis. These are taken to be the KS eigensystems of our DFT approach, leading to the electronic structure of Fig. 1(b,d). The KS wavefunctions, normalized to unity in the crystal volume Ω , are expressed as linear combinations of PWs that depend on the reciprocal lattice vectors \mathbf{G} associated to the replicated GNR lattices (Supporting Information, Sec. I and II). The correlation matrix elements are given by $\rho_{\nu\nu'}^{\mathbf{k}\mathbf{q}}(\mathbf{G}) = \langle \nu\mathbf{k} | e^{-i(\mathbf{q}+\mathbf{G})\cdot\mathbf{r}} | \nu'\mathbf{k} + \mathbf{q} \rangle$.

The population of single-particle levels is established by the Fermi-Dirac distribution $f_{\nu\mathbf{k}}$, which we evaluate by sampling temperatures from 300 to 900 K. The factor of 2 accounts for the spin degeneracy, while η is a small (positive) lifetime broadening parameter.³²

Polarization effects are activated by a test electron or photon with incident energy ω and in-plane momentum \mathbf{q} that weakly perturbs our systems. These effects are described by the density response function of *interacting* electrons, which can be obtained in the framework of TDDFT as:^{33,34} $\chi_{\mathbf{G}\mathbf{G}'} = \chi_{\mathbf{G}\mathbf{G}'}^0 + (\chi^0 v \chi)_{\mathbf{G}\mathbf{G}'}$.

In the RPA, one neglects short-range exchange-correlation effects by simply replacing the *unknown* v by the bare Coulomb terms $v_{\mathbf{G}\mathbf{G}'}^0 = 4\pi\delta_{\mathbf{G}\mathbf{G}'}/|\mathbf{q} + \mathbf{G}|^2$. A serious drawback stems from the long-range character of the Coulomb potential, which allows non-negligible interactions between repeated planar arrays even at large distances. To cut-off this unwanted phenomenon, we replace $v_{\mathbf{G}\mathbf{G}'}^0$ by the truncated Fourier integral:^{35–38}

$$v_{\mathbf{G}\mathbf{G}'} = \int_{-L/2}^{L/2} dz \int_{-L/2}^{L/2} dz' e^{iGz} \bar{v}_{\mathbf{g}\mathbf{g}'}^0(z, z') e^{-iG'z'}, \quad (2)$$

where $\bar{v}_{\mathbf{g}\mathbf{g}'}^0$ is the Fourier transform of $v_{\mathbf{G}\mathbf{G}'}^0$ along the out-of-plane axis, while \mathbf{g} and G denote the in-plane and out-of-plane components of \mathbf{G} .

Within linear response theory, the inelastic cross section corresponding to a process where the external perturbation creates an excitation of energy ω and wavevector $\mathbf{q} + \mathbf{G}$ is related to the diagonal elements of the inverse dielectric matrix $(\epsilon^{-1})_{\mathbf{G}\mathbf{G}'} = \delta_{\mathbf{G}\mathbf{G}'} + (v\chi)_{\mathbf{G}\mathbf{G}'}$. Collective

excitations (plasmons) are dictated by the zeros in the real part of the macroscopic dielectric function (permittivity), $\epsilon^M = 1/(\epsilon^{-1})_{00}$. The so-called Energy Loss (EL) function is proportional to the imaginary part of the inverse permittivity: $E_{\text{LOSS}} = -\text{Im}[(\epsilon^{-1})_{00}]$. Non-local field effects are included in E_{LOSS} through the off-diagonal elements of $\chi_{\mathbf{G}\mathbf{G}'}$.³⁹

The peculiar electronic structure of 4ZGNR (Fig. 1(b)) and 5AGNR (Fig. 1(d)), as compared to the well-known band dispersion of MG, is reflected in the EL spectra of the intrinsic systems, shown in Fig. 2. Undoped 4ZGNR and 5AGNR have two high-energy excitations (for $\omega > 3$ eV) that follow one-electron transitions connecting the \mathbf{k} -points with high DOS in the π - π^* , σ - π^* and π - σ^* bands. These are counterparts to the π and σ - π plasmons observed in intrinsic MG (Fig. 2(a,b)), few-layer graphene and graphite^{40–43}. Specifically, the π and π - σ structures of the GNRs exhibit a discontinuous dispersion vs \mathbf{q} and ω , as they are split into more branches (Fig. 2(c,d) and Fig. S2(c,d)).

This effect is due to the finite width of the GNRs in the periodic array that generates several one-dimensional bands of π and σ character. The number and dispersion of these bands is also strongly influenced by the GNR width, chirality and in-plane distance: the wider the ribbon the more regular the shape of the high-energy interband peaks, which approach the π and σ - π peaks of MG as the ribbon width tends to infinity (Fig. 2(a,b) and Fig. S2(a,b)). Then, the main designing ‘*ingredients*’ of the GNR arrays may be finely tuned to reach a specific energy for the π and σ - π excitations, which in turn may be used to change the response of a GNR-based device working in the VIS to UV regime.

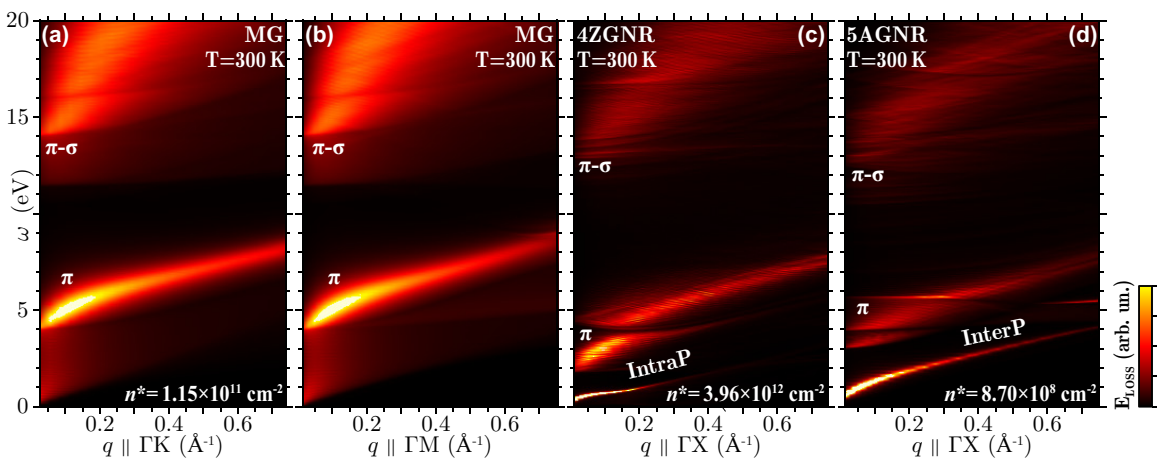


Figure 2. EL spectrum for intrinsic MG (a,b), 4ZGNR (c) and 5AGNR (d) at room temperature, i.e., E_{LOSS} vs $\omega < 20$ eV and $q < 0.8 \text{ \AA}^{-1}$. q is oriented along the 1st-BZ paths ΓK (a), ΓM (b) and ΓX (c,d). ‘IntraP’ and ‘InterP’ label the intraband and interband plasmons of 4ZGNR and 5AGNR, respectively. n^* is the concentration of conduction electrons.

The low-energy ends of the spectra (for $\omega < 3$ eV) exhibit an extra peak in both metallic and semiconducting GNRs, which is strictly absent in MG at the absolute

zero. This structure is more clearly visible in Fig. 3(a,e) and 4(a,e) below.

The large DOS value close to E_F in 4ZGNR (Fig. 1(b))

yields a concentration of $n^* = 3.96 \times 10^{12} \text{ cm}^{-2}$ conduction electrons, which allows the appearance of an intraband plasmon where the charge-carriers located on each ribbon of the array oscillate as a single two-dimensional (2D) gas (Figs. 2(c), 3(a), S2(c) and S3(a)). This observation is confirmed by the square-root-like dispersion for low q that is typical of 2D plasmons (Fig.S3(d)). The latter has been mostly observed in extrinsic MG⁴⁴, which even in the intrinsic case allows for a weak intraband contribution at room temperature due to a concentration of $n^* = 1.15 \times 10^{11} \text{ cm}^{-2}$ conduction electrons (Fig. S2(a,b)).

On the other hand, the energy gap at E_F in 5AGNR (Fig. 1(d)) yields a negligibly small intraband mode due to the tiny concentration of conduction electrons at room temperature ($n^* = 8.70 \times 10^8 \text{ cm}^{-2}$). The latter is not detectable in Figs. 2(d) and 4(a,d) but can be in principle characterized (Supporting Information, Sec. III). In contrast, an interband 2D plasmon is clearly recorded in the low-energy spectrum of 5AGNR, as testified by the intense signal in Figs. 2(d) and 4(a,d); this corresponds to a collective mode that is triggered by transitions between the valence and conduction DOS peaks at Γ (Fig. 1(d)).

The collective nature of the *newly* detected excitations

in 4ZGNR and 5AGNR is proved in Figs. 3(e) and 4(e), respectively, where we see that each excitation peak in the EL spectrum corresponds to a zero in the real permittivity $\text{Re}(\epsilon^M)$, at a frequency where the imaginary permittivity $\text{Im}(\epsilon^M)$ is small.

These excitations are indeed genuine plasmons, which can be used in practical THz applications. Moreover, as is the case for the high-energy π excitations, these low-energy modes arise from transitions involving the π bands, which means that their intensities and energy-momentum dispersions can be modulated according to external factors that change the band levels, such as the already mentioned ribbon width, in-plane distance and chirality.

Let us now see how the dielectric properties of the GNR arrays behave with injecting/ejecting electrons by doping or gating. Extrinsic systems are simulated here by slightly changing the level populations in Eq. (1), in such a way that band dispersions and single-particle KS orbitals are negligibly altered by the applied variations of the $f_{\nu\mathbf{k}}$ -factors. For doping levels ΔE_F not larger than $\sim 1 \text{ eV}$ the high-energy end ($\omega > 3 \text{ eV}$) of our EL spectra is practically unaffected. On the contrary, unprecedented new features are recorded at the low-energy end ($\omega < 3 \text{ eV}$).

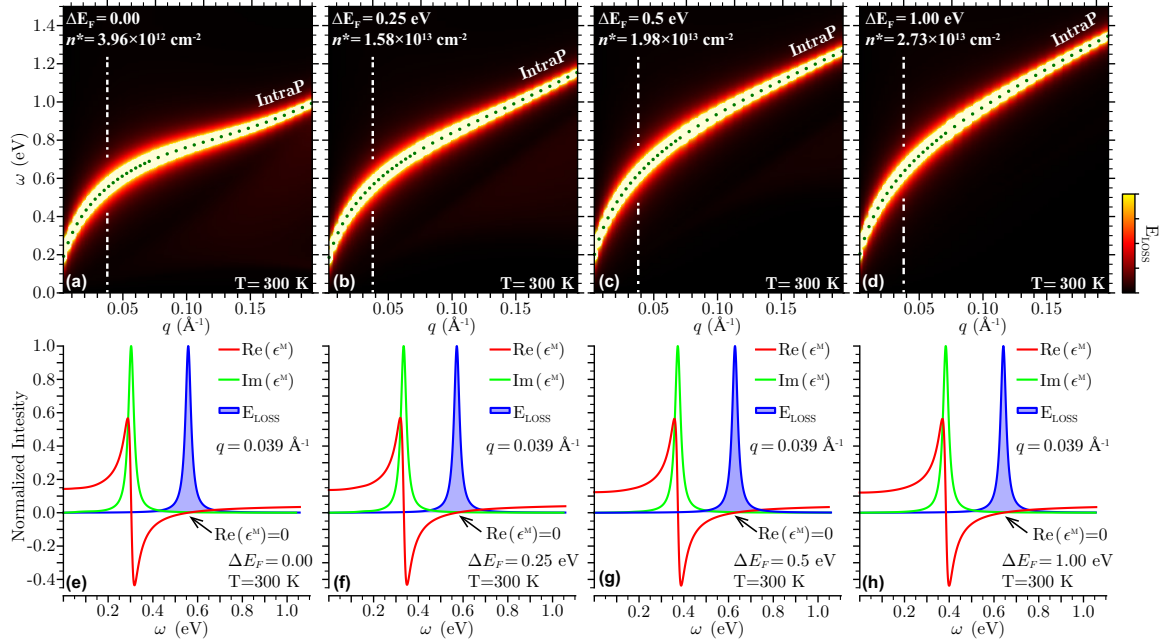


Figure 3. EL spectrum and complex permittivity of intrinsic and extrinsic 4ZGNRs at room temperature. (a-d) E_{Loss} vs $\omega < 1.5 \text{ eV}$ and $q < 0.11 \text{ \AA}^{-1}$. (e-h) $\text{Re}(\epsilon^M)$, $\text{Im}(\epsilon^M)$ and E_{Loss} vs $\omega < 1.5 \text{ eV}$ at $q = 0.039 \text{ \AA}^{-1}$. In (a-d) the same color code/intensity scale as in Fig. 2 is used, with the dark green dots denoting the (ω, q) -dispersion of the intraband plasmon (IntraP), and n^* being the concentration of conduction electrons. The vertical grid-lines mark the q value used in the plots of (e-h), where ϵ^M and E_{Loss} are normalized to $\max[\text{Im}(\epsilon^M)]$ and $\max[-\text{Im}(\epsilon_{00}^{-1})]$, respectively.

In Fig. 3(a-d) we show the low- ω and low- q region of the EL spectrum of the 4ZGNR array, zooming on the undoped case ($\Delta E_F = 0$) and analyzing three positive

doping levels, namely $\Delta E_F = 0.25, 0.5, 1.0 \text{ eV}$ (see also Fig. S3(a-c)). In all cases, we observe a single dispersive structure, the intraband plasmon, which is a genuine col-

lective mode, with the EL peak corresponding to a zero in $\text{Re}(\epsilon^M)$ and a small value of $\text{Im}(\epsilon^M)$ (Fig. 3(e-h)). We also notice minor differences in the four EL spectra, with the plasmon energy slightly increasing with increasing ΔE_F (Fig. S3(d)).

More interesting features are observed in doped arrays of 5AGNR, whose low- ω and low- q response is shown in Fig. 4. In the undoped case ($\Delta E_F = 0$) a single dispersive peak is detected in the EL spectrum, which represents an interband plasmon following coherent electronic excitations between the VB and CB (Fig. 4(a,d) and Fig. S4(c)). When a small doping is introduced ($\Delta E_F = -0.2, 0.3$ eV) the conduction electron/valence hole concentration bursts from $\pm 10^9$ to $\pm 10^{12}$ cm^{-2} , and another dispersive peak appears in the EL spectrum due to a clearly resolved intraband plasmon (Fig. 4(b,c,f,g) and Fig. S4(b,e)). For these low wavevectors ($q < 0.02$ \AA^{-1}), the intraband mode is the most intense contribution, while the interband plasmon is depressed because the doping partially fills the CB near Γ

thus inhibiting quasi-vertical ($q \rightarrow 0, \omega$) interband transitions. In the $0.02 < q < 0.06$ \AA^{-1} region, both intraband and interband plasmons coexist. At larger values of q , the interband plasmon becomes the most intense peak while the intraband plasmon is strongly damped. A slightly larger value of the doping ($\Delta E_F = 0.4$ eV) leads to an even more intriguing situation: the single dispersive peak visible in Fig. 4(d,h) has a **double nature**, as testified by the kink in peak dispersion and the abrupt decrease in intensity (increase in width) found at $q \sim 0.05$ \AA^{-1} (see also Fig. S4(f)). Indeed, interband transitions between the high-DOS points of Fig. 1(d) for $q < 0.04$ \AA^{-1} are strongly quenched by electron population of conduction levels; thus, the intense peak showing the \sqrt{q} dispersion is mostly originated by the intraband plasmon. Conversely, for $q > 0.04$ \AA^{-1} the intraband plasmon enters a region where it is damped by interband transitions; as a result, most of the spectral weight is concentrated on the interband plasmon, while the overdamped intraband plasmon only appears as a faint peak.

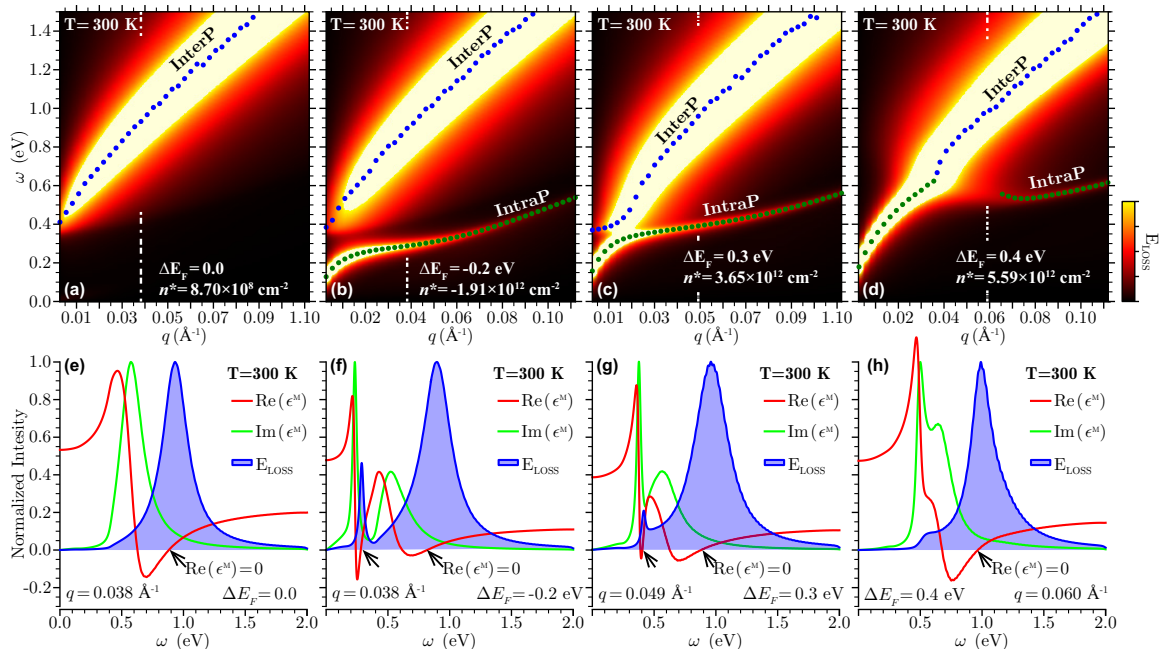


Figure 4. Dielectric response and plasmon dispersions of intrinsic and extrinsic 5AGNRs at $T = 300$ K. (a-d) E_{LOSS} vs $\omega < 1.5$ eV and $q < 0.11$ \AA^{-1} with the same intensity scale as Figs. 2 and 3(a-d). The blue and dark green dots mark the interband (InterP) and intraband (IntraP) plasmon (ω, q)-dispersions, respectively. n^* is the concentration of valence holes (-)/conduction electrons (+). The vertical grid-lines mark the q values used in the plots of (e-h), where ϵ^M and E_{LOSS} are normalized as in Fig. 3(e-h)

Another remarkable effect is the high sensitivity of the intraband plasmon to the type of doping; opposite doping levels, such as the $\Delta E_F = \pm 0.2$ and $\Delta E_F = \pm 0.3$ values shown in Fig. 5(a), produce significantly different charge-carrier concentrations and plasmon dispersion curves for energies larger than 0.1 eV and transferred momenta above 0.02 \AA^{-1} . Such a sensitivity is ascribed to the slight asymmetry of the valence and conduction

electron levels of 5AGNR close to band gap (inset in Fig. 1(d)). On the other hand, the interband plasmon is much less influenced by the doping type, because the valence and conduction DOS peaks have similar intensities (Fig. S4(h)). In the lower THz region, interband transitions are forbidden by the band gap, while the intraband plasmon follows an ω vs q dispersion that is consistent with the semi-phenomenological relation 23

$\omega = \text{Re}(\sqrt{2\pi n^* q / m^* - \eta^2} - i\eta)$, where $m^* = 0.36$ au is the effective mass of conduction electrons in 5AGNR. Indeed, the analytical dispersions are suitable for doped GNR arrays of 10-100 nm width (Supporting Information, Sec. III). Nevertheless, they turn out to be amazingly similar to our TDDFT dispersions for $\Delta E_F < 0.5$ eV (Fig. 5(b) and S5(b,c)).

As a final remark we observe that in semiconducting GNRs, due to their small band gap, the temperature plays a role in dictating the populations of the VB and

CB (Supporting Information, Sec. IV). Accordingly, the intraband plasmon mode can be triggered by working at temperatures larger than ~ 500 K, which may have a crucial role in relation with power consumption of nanodevices (Fig. 5(c,d) and Fig. S6). Charge carrier concentrations generated by temperature increase are nevertheless much smaller than those obtained with doping or gating. For this reason, no particular interference is recorded in Fig. 5(c,d) (and Fig. S6) between intraband and interband plasmon modes.

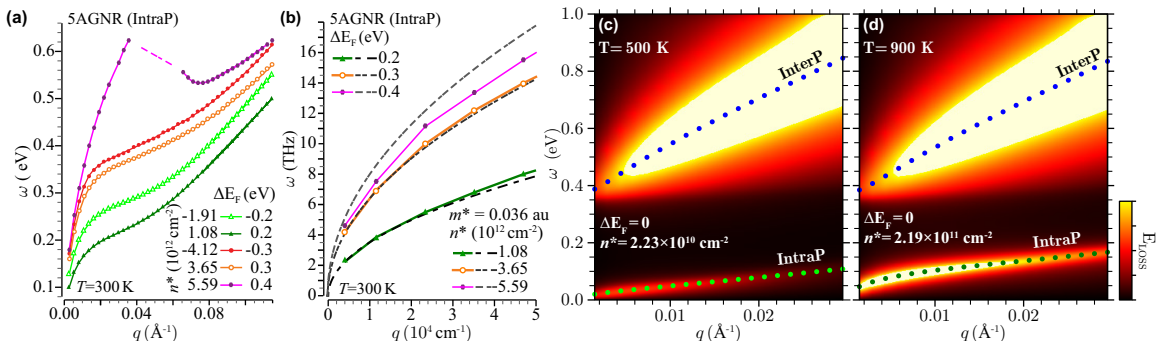


Figure 5. (a) Intraband plasmon dispersions for 5AGNR at $T = 300$ K with doping levels $|\Delta E_F| \leq 0.4$ eV. (b) Intraband plasmon dispersions for 5AGNR at $T = 300$ K in the lower THz range; our TDDFT results are compared with the semi-phenomenological curves of Ref. 23 (dashed lines), which depend on the effective mass m^* and concentration n^* of electrons in the conduction band. (c,d) E_{Loss} vs $\omega < 1$ eV and $q < 0.03 \text{ \AA}^{-1}$ at $T = 500, 900$ K with the same settings/intensity scale as Figs. 2, 3(a-d) and 4(a-d).

In summary, we have discussed the dielectric properties and plasmon dispersions in 2D arrays of GNRs scrutinizing the excitation energy regime going from the THz to the UV scale. At VIS to UV frequencies, we have found the two standard interband excitations of carbon-based materials, namely the π and σ - π plasmons, with the π plasmon being strongly influenced by the GNR geometry. On the THz regime, we have detected *new* collective modes of different nature. Semimetallic GNRs display an intraband 2D plasmon with large intensity relative to the high-energy plasmons even in the intrinsic case. Semiconducting GNRs experience a fascinating interplay of intraband and interband collective modes, whose relative intensities and dispersions are strongly influenced by the actual occupation of single-particle levels near the Fermi energy. This strong sensitivity allows for a high tunability and control of the new plasmons. Indeed, nano-infrared imaging measurements in patterned GNRs on Al_2O_3 ¹⁷ have revealed the appearance of an *edge* (interband) plasmon superimposed to a *conventional* (intraband) plasmon. The two modes are well resolved in space on GNR samples of 480 nm width at a working frequency of ~ 0.15 eV with a doping level of ~ 0.3 eV. In our narrow-width GNR, the interband and intraband features can be resolved in momentum space, only.

Our calculations demonstrate that it is possible to construct new materials with plasmonic resonances that are tunable to suit a specific demand in both the VIS-UV

and THz regimes, by means of chemical doping, electronic gating, and also by means of a careful choice of the geometry. These findings if confirmed by further experiments would widen the perspectives on applications of GNR arrays for the engineering of nanophotonic and nanoelectronic devices.

ACKNOWLEDGMENTS

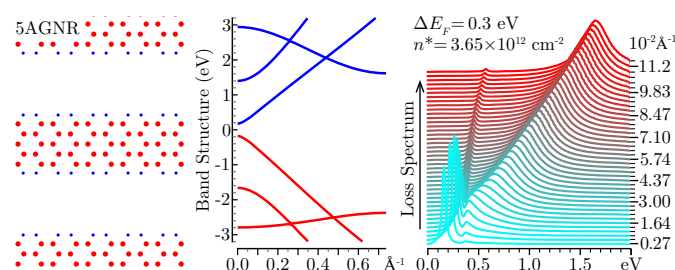
C.V.G. acknowledges the financial support of “*Secretaría Nacional de Educación Superior, Ciencia, Tecnología e Innovación*” (SENESCYT-ECUADOR). All authors thank Dr V.M. Silkin from the University of the Basque Country for his precious support in developing the TDDFT code.

REFERENCES

- Lin, Y.-M.; Jenkins, K. A.; Valdes-Garcia, A.; Small, J. P.; Farmer, D. B.; Avouris, P. *Nano Lett.* **2009**, *9*, 422-426.
- Shuba, M. V.; Slepian, G. Y.; Maksimenko, S. A.; Thomsen, C.; Lakhtakia, A. *Phys. Rev. B* **2009**, *79*, 155403.
- Bao, Q.; Loh, K. P. *ACS Nano* **2012**, *6*, 3677-3694.
- Sensale-Rodriguez, B.; Yan, R.; Kelly, M. M.; Fang, T.; Tahy, K.; Hwang, W. S.; Jena, D.; Liu, L.; Xing, H. G. *Nature communications* **2012**, *3*, 780.
- Garcia de Abajo, F. J. *Acs Photonics* **2014**, *1*, 135-152.

- ⁶Brun, C.; Wei, T. C.; Franck, P.; Chong, Y. C.; Congxiang, L.; Leong, C. W.; Tan, D.; Kang, T. B.; Coquet, P.; Baillargeat, D. *IEEE Trans. THz Sci. Technol.* **2015**, *5*, 383.
- ⁷Neto, A. C.; Guinea, F.; Peres, N.; Novoselov, K. S.; Geim, A. K. *Rev. Mod. Phys.* **2009**, *81*, 109.
- ⁸Ju, L.; Geng, B.; Horng, J.; Girit, C.; Martin, M.; Hao, Z.; Bechtel, H. A.; Liang, X.; Zettl, A.; Shen, Y. R.; Wang, F. *Nature Nanotechnology* **2011**, *6*, 630–634.
- ⁹Zhou, W.; Lee, J.; Nanda, J.; Pantelides, S. T.; Pennycook, S. J.; Idrobo, J.-C. *Nature Nanotechnology* **2012**, *7*, 161–165.
- ¹⁰Yan, H.; Low, T.; Zhu, W.; Wu, Y.; Freitag, M.; Li, X.; Guinea, F.; Avouris, P.; Xia, F. *Nature Photonics* **2013**, *7*, 394–399.
- ¹¹Liou, S. C.; Shie, C.-S.; Chen, C. H.; Breitwieser, R.; Pai, W. W.; Guo, G. Y.; Chu, M.-W. *Phys. Rev. B* **2015**, *91*, 045418.
- ¹²Cupolillo, A.; Politano, A.; Ligato, N.; Perez, D. C.; Chiarello, G.; Caputi, L. *Surface Science* **2015**, *634*, 76–80.
- ¹³Christensen, J.; Manjavacas, A.; Thongrattanasiri, S.; Koppens, F. H.; Garcia de Abajo, F. J. *ACS Nano* **2011**, *6*, 431–440.
- ¹⁴Woessner, A.; Lundberg, M. B.; Gao, Y.; Principi, A.; Alonso-Gonzalez, P.; Carrega, M.; Watanabe, K.; Taniguchi, T.; Vignale, G.; Polini, M.; Hone, J.; Hillenbrand, R.; Koppens, F. H. L. *Nature Materials* **2015**, *14*, 421–425.
- ¹⁵Tong, J.; Muthee, M.; Chen, S.-Y.; Yngvesson, S. K.; Yan, J. *Nano Lett.* **2015**, *15*, 5295–5301.
- ¹⁶Nikitin, A. Y.; Guinea, F.; Garcia-Vidal, F. J.; Martin-Moreno, L. *Phys. Rev. B* **2012**, *85*, 081405.
- ¹⁷Fei, Z.; Goldflam, M. D.; Wu, J.-S.; Dai, S.; Wagner, M.; McLeod, A. S.; Liu, M. K.; Post, K. W.; Zhu, S.; Janssen, G. C. A. M.; Fogler, M. M.; Basov, D. N. *Nano Lett.* **2015**, *15*, 8271–8276.
- ¹⁸Son, Y.-W.; Cohen, M. L.; Louie, S. G. *Phys. Rev. Lett.* **2006**, *97*, 216803.
- ¹⁹Yang, L.; Park, C.-H.; Son, Y.-W.; Cohen, M. L.; Louie, S. G. *Phys. Rev. Lett.* **2007**, *99*, 186801.
- ²⁰Dubois, S. M. M.; Zanolli, Z.; Declerck, X.; Charlier, J. C. *Eur. Phys. J. B* **2009**, *72*, 1–24.
- ²¹Kan, E.-j.; Li, Z.; Yang, J.; Hou, J. *Journal of the American Chemical Society* **2008**, *130*, 4224–4225.
- ²²Tao, C.; Jiao, L.; Yazzev, O. V.; Chen, Y.-C.; Feng, J.; Zhang, X.; Capaz, R. B.; Tour, J. M.; Zettl, A.; Louie, S. G.; Dai, H.; Crommie, M. F. *Nature Physics* **2011**, *7*, 616–620.
- ²³Popov, V. V.; Bagaeva, T. Y.; Otsuji, T.; Ryzhii, V. *Phys. Rev. B* **2010**, *81*, 073404.
- ²⁴Andersen, D. R.; Raza, H. *Phys. Rev. B* **2012**, *85*, 075425.
- ²⁵Perdew, J. P.; Zunger, A. *Phys. Rev. B* **1981**, *23*, 5048.
- ²⁶Troullier, N.; Martins, J. L. *Phys. Rev. B* **1991**, *43*, 1993.
- ²⁷Gonze, X.; dum, d.; dum, d.; dum, d.; dum, d.; dum, d.; dum, d.; dum, d.; dum, d.; dum, d.; dum, d.; dum, d. *Computer Physics Communications* **2009**, *180*, 2582–2615.
- ²⁸Monkhorst, H. J.; Pack, J. D. *Phys. Rev. B* **1976**, *13*, 5188.
- ²⁹Adler, S. L. *Phys. Rev.* **1962**, *126*, 413.
- ³⁰Wiser, N. *Phys. Rev.* **1963**, *129*, 62.
- ³¹Kubo, R. *Journal of the Physical Society of Japan* **1957**, *12*, 570–586.
- ³²Silkin, V. M.; Chulkov, E. V.; Echenique, P. M. *Phys. Rev. B* **2003**, *68*, 205106.
- ³³Petersilka, M.; Gossmann, U. J.; Gross, E. K. U. *Phys. Rev. Lett.* **1996**, *76*, 1212–1215.
- ³⁴Onida, G.; Reining, L.; Rubio, A. *Rev. Mod. Phys.* **2002**, *74*, 601.
- ³⁵Despoja, V.; Dekanić, K.; Šunjić, M.; Marušić, L. *Phys. Rev. B* **2012**, *86*, 165419.
- ³⁶Despoja, V.; Novko, D.; Dekanić, K.; Šunjić, M.; Marušić, L. *Phys. Rev. B* **2013**, *87*, 075447.
- ³⁷Novko, D.; Despoja, V.; Šunjić, M. *Phys. Rev. B* **2015**, *91*, 195407.
- ³⁸Pisarra, M.; Sindona, A.; Gravina, M.; Silkin, V. M.; Pitarke, J. M. *Phys. Rev. B* **2016**, *93*, 035440.
- ³⁹Kramberger, C.; Hambach, R.; Giorgetti, C.; Rummeli, M. H.; Knupfer, M.; Fink, J.; Büchner, B.; Reining, L.; Einarsson, E.; Maruyama, S.; Sottile, F.; Hannewald, K.; Olevano, V.; Marinopoulos, A. G.; Pichler, T. *Phys. Rev. Lett.* **2008**, *100*, 196803.
- ⁴⁰Eberlein, T.; Bangert, U.; Nair, R. R.; Jones, R.; Gass, M.; Bleloch, A. L.; Novoselov, K. S.; Geim, A.; Briddon, P. R. *Phys. Rev. B* **2008**, *77*, 233406.
- ⁴¹Wachsmuth, P.; Hambach, R.; Kinyanjui, M. K.; Guzzo, M.; Benner, G.; Kaiser, U. *Phys. Rev. B* **2013**, *88*, 075433.
- ⁴²Wachsmuth, P.; Hambach, R.; Benner, G.; Kaiser, U. *Phys. Rev. B* **2014**, *90*, 235434.
- ⁴³Taft, E. A.; Philipp, H. R. *Phys. Rev.* **1965**, *138*, A197–A202.
- ⁴⁴Pisarra, M.; Sindona, A.; Riccardi, P.; Silkin, V. M.; Pitarke, J. M. *New Journal of Physics* **2014**, *16*, 083003.

GRAPHICAL ABSTRACT



ASSOCIATED CONTENT

Supporting Information: DFT calculations, geometry optimizations (Sec. I); TDDFT scheme, intrinsic GNRs (Sec. II); doped GNRs, interband and intraband plasmon dispersions (Sec. III); temperature effects (Sec. IV) (PDF)

AUTHOR INFORMATION

Corresponding

*antonello.sindona@fis.unical.it

Author

Supporting Information: The main text has been concerned with the dielectric response of two narrow-size graphene nanoribbons (GNRs), organized in periodic planar arrays with the zigzag (Z) and armchair (A) geometries. These GNRs are conventionally denoted 4ZGNR and 5AGNR, respectively¹⁸. Time-dependent density-functional theory has been carried out for both intrinsic (undoped) and extrinsic (doped, gated) systems within the random phase approximation (RPA). Energy loss spectra have been represented as density plots vs frequency ω and transferred momentum q parallel to the GNR axis. These supplementary notes are organized as follows: Sec. I provides the details on ground state computations and geometry optimizations for the 4ZGNR and 5AGNR arrays; Sec. II deals with the calculations of the plasmon structure of the intrinsic systems in comparison with that of pristine graphene; Sec. III gives some additional arguments on the effect of doping in 4ZGNR and 5AGNR, focussing on the (ω, q) -dispersion of the intraband and interband plasmons; the semiclassical limit of the approach is validated by zooming on the lower THz region;

I. LOCAL DENSITY CALCULATIONS AND GEOMETRY OPTIMIZATION

Density functional calculations were performed using the plane-wave (PW) basis set²⁷, represented by the space functions $\text{PW}_{\mathbf{k}+\mathbf{G}}(\mathbf{r}) = \Omega_0^{-1/2} e^{i(\mathbf{k}+\mathbf{G})\cdot\mathbf{r}}$, where \mathbf{k} is a wavevector in the first Brillouin zone (1stBZ), \mathbf{G} a

reciprocal vector, and Ω_0 denotes the unit-cell volume of the real-space lattice. The number of PWs was limited by the cut-off condition: $|\mathbf{k} + \mathbf{G}|^2/2 < 25$ Hartree.

The local density approximation (LDA) was used, as parametrized by the Perdew-Zunger form of the uniform-gas correlation energy²⁵. Norm-conserving pseudo-potentials of the Troullier-Martins type²⁶ were adopted.

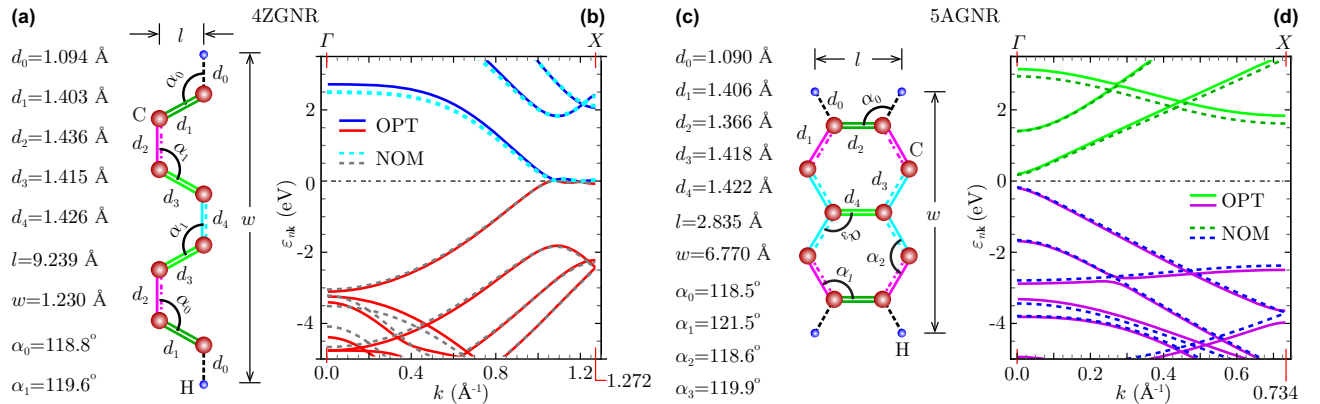


Figure S1. Optimized unit cells (a,c) and LDA electronic structure (b,d) for 4ZGNR (a,b) and 5AGNR (c,d). In (a,c), the different bond-lengths and angles are denoted d_0, \dots, d_4 and $\alpha_0, \dots, \alpha_3$, respectively; w labels the cell-width and l the cell-length; the C-H bond-length approximates to 1.09 Å; the average C-C bond length equals to 1.419 Å in 4ZGNR (a) and 1.404 Å in 5AGNR (c). In (b,d), the band-levels from the optimized (OPT) unit cells of (a,c) are compared with those resulting from the nominal (NOM) cells of Fig. 1(a,c), which are plotted in Fig. 1(b,d) of the main text.

The basic parameters of the unit cells of 4ZGNR and 5AGNR, i.e., the C-C and C-H bond lengths and angles, were determined by geometry optimization using the Broyden-Fletcher-Goldfarb-Shanno method^{45–48}. The resulting average C-C and C-H distances turned out to be slightly different from the nominal values of 1.42 and 1.09 Å, respectively, used in the main text to generate the non optimized structures of Fig. 1(a,c).

Periodic planar arrays of 4ZGNR and 5AGNR were then generated with both the optimized and non-optimized unit cells assuming an in-plane vacuum distance of 15 Å. The three-dimensional (3D) periodicity required by PW-DFT was set by replicating the GNR arrays with an out of plane lattice constant of 15 Å, corresponding to the unit-cell volumes $\Omega_0 \sim 950 \text{ \AA}^3$ for 4ZGNR and $\Omega_0 \sim 1470 \text{ \AA}^3$ for 5AGNR.

Both geometry optimization and ground state calculations were carried out using an unshifted Monkhorst-Pack (MP) grid²⁸ made of $N_{\mathbf{k}} = 60 \times 1 \times 1$ wavevectors, resulting in a uniform one-dimensional (1D) sampling of the irreducible segment of the 1stBZ.

The band energies obtained with the optimized cells (denoted OPT in Fig. S1(b,d)) were found to differ negligibly from those of the non optimized structures (denoted NOM in Fig. S1(b,d) and taken from Fig. 1(b,d) of the main text). Regular planar arrays made of wider ribbons were tested as well (though not reported here) for more systematic future studies.

Electronic structure calculations were also run on monolayer graphene (MG) for comparison purposes (see Fig. 2 and Fig. S2). In this case the honeycomb lattice structure of C atoms (separated by a nearest neighbor

distance of 1.42 Å) was replicated with an out-of-plane vacuum distance of 15 Å, i.e., a unit-cell volume $\Omega_0 \sim 110 \text{ \AA}^3$. The 1stBZ of the two-dimensional (2D) material was represented on an MP grid of $N_{\mathbf{k}} = 60 \times 60 \times 1$ \mathbf{k} -points.

II. INTRINSIC SYSTEMS

Energy Loss (EL) calculations in the main text were based on the ‘*nominal*’ cells reported in Fig. 1(a,c) that have a more balanced space symmetry group with respect to the optimized cells of Fig S1(a,c). With this choice, the computational burden required to sample the KS structure of the systems is reduced to the analysis of the $k_{\geq 0}$ part of the 1st BZ, ended by the Γ and X points (that are shown in Figs. 1(b,d) and S1(b,d)).

In the ΓX domain, we calculated the KS energies $\varepsilon_{\nu\mathbf{k}}$ and wavefunctions

$$\langle \mathbf{r} | \nu \mathbf{k} \rangle = N_{\mathbf{k}}^{-1/2} \sum_{\mathbf{G}} c_{\nu\mathbf{k}+\mathbf{G}} \text{PW}_{\mathbf{k}+\mathbf{G}}(\mathbf{r}), \quad (\text{S3})$$

being normalized to unity in the crystal volume $\Omega = N_{\mathbf{k}}\Omega_0$, with the \mathbf{G} -sum limited by the cut-off condition set forth above.

The full plasmon structure of the intrinsic GNRs was explored at frequencies $\omega \leq 20$ eV (Fig. 2(c,d) and S2(c,d)). Transferred momentum values q parallel to the GNR axis were considered in the range of ~ 0.02 to $\sim 0.8 \text{ \AA}^{-1}$.

The converged ground state density $n(\mathbf{r}) = \sum_{\nu\mathbf{k} \text{ occ}} |\langle \mathbf{r} | \nu \mathbf{k} \rangle|^2$ was determined with ~ 15000 PW-coefficients $\{c_{\nu\mathbf{k}+\mathbf{G}}\}$ per occupied wavefunction, leading to the electronic structure of Fig. 1(b,d). $n(\mathbf{r})$ was subsequently used in a non self-consistent run to determine the KS energies and wavefunctions on an MP mesh of $N_{\mathbf{k}}$ of $180 \times 1 \times 1$ \mathbf{k} -points. 120 bands (indexed by ν) were included to have a reliable dielectric response in the considered frequency and transferred momentum ranges.

EL calculations for MG were run on an MP-grid of $N_{\mathbf{k}} = 180 \times 180 \times 1$ wavevectors in the irreducible 1st BZ of the 2D material, including 80 bands and ~ 5000 PW-coefficients per wavefunction (Fig. 2(a,b) and S2(a,b)).

The non interacting density-density response (or unperturbed susceptibility) $\chi_{\mathbf{G}\mathbf{G}'}^0$ was computed for MG, 4ZGNR, and 5AGNR at room temperature. As reported in Eq. (1) of the main text, $\chi_{\mathbf{G}\mathbf{G}'}$ includes all possible one-electron processes between occupied and empty band levels, separated in energy by $\varepsilon_{\nu\mathbf{k}} - \varepsilon_{\nu'\mathbf{k}+\mathbf{q}}$. The dynamical screening features are provided by the retarded Green’s functions $(\omega + \varepsilon_{\nu\mathbf{k}} - \varepsilon_{\nu'\mathbf{k}+\mathbf{q}} + i\eta)^{-1}$, which contains the positive infinitesimal η . Transition rates between the band levels are made of products of correlation matrix

elements

$$\begin{aligned} \rho_{\nu\nu'}^{\mathbf{k}\mathbf{q}}(\mathbf{G}) &= \int_{\Omega} d^3r \langle \nu \mathbf{k} | \mathbf{r} \rangle e^{-i(\mathbf{q}+\mathbf{G})\cdot\mathbf{r}} \langle \mathbf{r} | \nu' \mathbf{k} + \mathbf{q} \rangle \\ &= \sum_{\mathbf{G}'} c_{\nu\mathbf{k}-\mathbf{G}+\mathbf{G}'} c_{\nu'\mathbf{k}+\mathbf{q}+\mathbf{G}'}, \end{aligned} \quad (\text{S4})$$

weighted by the Fermi-Dirac factors $f_{\nu\mathbf{k}} - f_{\nu'\mathbf{k}+\mathbf{q}}$.

The unperturbed susceptibility of 4ZGNR and 5AGNR was represented with 121 reciprocal lattice vectors, sorted in length and cut-off by the condition: $|\mathbf{G}| = \sqrt{|\mathbf{g}|^2 + G^2} < 7.2 \text{ \AA}^{-1}$, with \mathbf{g} and G denoting the in-plane and out-of-plane components of \mathbf{G} , respectively. 60 transferred momentum values were sampled along ΓX , and 3001 frequencies below 20 eV. η was replaced with a (finite) lifetime broadening parameter of 0.02 eV.

The unperturbed susceptibility of MG was represented with 50 reciprocal lattice vectors, being such that $|\mathbf{G}| < 3.2 \text{ \AA}^{-1}$.⁴⁴ The ΓK and ΓM high-symmetry paths were sampled with 60 and 90 q -values, respectively. 3001 ω -values below 30 eV were selected with $\eta = 0.02$ eV.

Accordingly, unperturbed susceptibility matrices were generated for all sampled frequencies and transferred momenta. With the $\chi_{\mathbf{G}\mathbf{G}'}^0$ matrices at hand, the interacting density-density response function (susceptibility) $\chi_{\mathbf{G}\mathbf{G}'}$ was obtained from the central equation of TDDFT (see main text). The latter is a Dyson-like equation, which can be rewritten as

$$\chi_{\mathbf{G}\mathbf{G}'} = \chi_{\mathbf{G}\mathbf{G}'}^0 + \sum_{\mathbf{G}''\mathbf{G}'''} \chi_{\mathbf{G}\mathbf{G}''}^0 v_{\mathbf{G}''\mathbf{G}'''} \chi_{\mathbf{G}''\mathbf{G}'}^0, \quad (\text{S5})$$

by making explicit the summation indices.

The effective potential matrix elements in Eq. (S5) may be calculated from the truncated Fourier integrals given in Eq. (2), which yields

$$\begin{aligned} v_{\mathbf{G}\mathbf{G}'} &= \frac{4\pi\delta_{\mathbf{G}\mathbf{G}'}}{|\mathbf{q} + \mathbf{G}|^2} + \frac{4\pi\delta_{\mathbf{G}\mathbf{G}'} e^{-iL_z \frac{G-G'}{2}}}{L_z |\mathbf{q} + \mathbf{G}|} \\ &\times \frac{1 - e^{-L_z |\mathbf{q}+\mathbf{G}|}}{G^2 + |\mathbf{q} + \mathbf{G}|^2} \frac{GG' - |\mathbf{q} + \mathbf{G}|^2}{G'^2 + |\mathbf{q} + \mathbf{G}|^2}. \end{aligned} \quad (\text{S6})$$

The $v_{\mathbf{G}\mathbf{G}'}$ terms have been proved to efficiently cut-off the spurious interaction between replicas of planar graphene-based systems³⁵⁻³⁸.

Finally, the EL spectra were computed by

$$E_{\text{LOSS}} = -\text{Im} \sum_{\mathbf{G}} v_{0\mathbf{G}} \chi_{\mathbf{G}0}, \quad (\text{S7})$$

where

$$\chi_{\mathbf{G}\mathbf{G}'} = \sum_{\mathbf{G}''} [(1 - \chi^0 v)^{-1}]_{\mathbf{G}\mathbf{G}''} \chi_{\mathbf{G}''\mathbf{G}'}^0, \quad (\text{S8})$$

is the solution of Eq. (S5).

Fig. S2 provides a complementary view to Fig. 2, with the EL spectra of MG, 4ZGNR and 5AGNR being reported for selected q values in the corresponding transferred momentum domains. As pointed out in the main

text, the one-peak structure of the π and σ - π plasmons in MG is turned into well resolved sub-peak structures in the GNRs. These originate from the several π and σ bands of the 1D materials (Figs. 1(b,d) and S1(b,d)).

The low-energy intraband and interband modes for 4ZGNR and 5AGNR, respectively, appear to be well resolved and have higher intensities with respect to the π and σ - π modes. In particular the intraband mode of 4ZGNR is generated by a conduction-electron concentra-

tion n^* of $3.96 \times 10^{12} \text{ cm}^{-2}$ (Fig. 2(c)).

Such a mode is absent in MG at the absolute zero because of the vanishing behavior of the density of states (DOS) at the inequivalent K points of the 1st BZ. The change in the Fermi-Dirac statistics at room temperature leads to the conduction-electron concentration $n^* = 1.15 \times 10^{11} \text{ cm}^{-2}$ (Fig. 2(a,b)), which in turns is responsible for a weak structure in the optical region of MG. This is barely visible at the lowest q 's in the plots of Fig. S2(a,b).

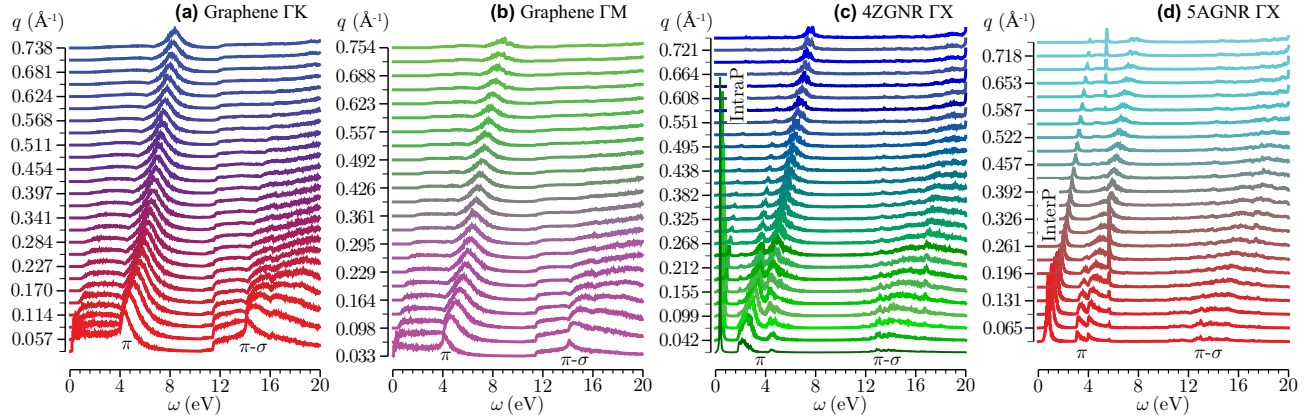


Figure S2. E_{LOSS} for intrinsic MG (a,b), 4ZGNR (c) and 5AGNR (d) at $T = 300 \text{ K}$, corresponding to some of the sampled momenta in the range of 0.02 to 0.8 \AA^{-1} along the ΓK (a), ΓM (b) and ΓX (c,d) directions of the relative 1st BZs. The EL curves are represented in a frequency region below 20 eV , and shifted vertically for clarity.

III. DOPED SYSTEMS

To explore the dielectric properties of the GNRs at infrared frequencies, we used an MP mesh of $N_{\mathbf{k}} = 1000 \times 1 \times 1$ wavevectors with ~ 30 bands, covering the frequency region $\omega \leq 2 \text{ eV}$.

Besides the dielectric properties of the pristine GNR arrays, we also studied how these properties change with doping. Indeed doping can happen as an unwanted effect due to chemical contamination or it can be introduced in a controlled way, i.e., after functionalization of the GNR or through a gating potential. Doping or gating was simulated by changing the occupation factors $f_{\nu\mathbf{k}}$ and $f_{\nu\mathbf{k}+\mathbf{q}}$ in $\chi_{\mathbf{G}\mathbf{G}'}^0$ (see Eq. (1)), according to the concentration of injected/ejected electrons. It can be safely assumed that the doping values sampled in this work have a negligible effect on the KS electronic structure^{38,44}. All other settings were the same as for the intrinsic systems.

Figs. S3 and S4 provide a complementary representation of the EL properties of 4ZGNR, given in Fig. 3(a-d), and 5AGNR, reported in Fig. 4 (a-d), respectively.

In semi-metals like mono and bilayer graphene, even a small doping yields the formation of a quasi-2D gas of charge carriers (electrons or holes). The fact that the CB (VB) becomes partially occupied (unoccupied) causes the appearance of low-energy intraband single-

particle transitions and collective excitations; the doping also causes the opening of a gap for interband transitions at low momenta.

In 4ZGNR, the non vanishing DOS at the Fermi level (Fig. 1(b)) causes the appearance of a well resolved intraband mode being weakly affected by the doping (gating). As shown in Fig. S3(d), the plasmon resonance energies slightly increase with increasing the injected electron concentration, following the typical square-root-like dispersion of the 2D plasmon in MG as $q \rightarrow 0$. These features are separately visible in Fig. 3(a-d).

It is worth mentioning that the effective charge carrier density contributing to the intraband mode in 4ZGNR is of the same order of magnitude for all sampled doping levels, i.e., 10^{13} cm^{-2} . Therefore, moderate energy shifts, up to 0.5 eV , are recorded in the intraband plasmon dispersions (Fig. S3(d)). In contrast, doping levels of 0.5 and 1 eV in MG lead to a more pronounced charge carrier density increase, of 10^{13} and 10^{14} cm^{-2} , respectively. Accordingly, a substantial variation in the plasmon energy of the extrinsic 2D plasmon of MG has been reported.⁴⁴

In 5AGNR, the presence of a small gap with high DOS (Fig. 1(d)) allows the appearance of an interband plasmon that appears to be weakly influenced by electron injection/ejection. On the other hand, positive/negative Fermi energy shifts generate an intraband plasmon that is extremely sensitive to the doping level and may interfere with the interband plasmon.

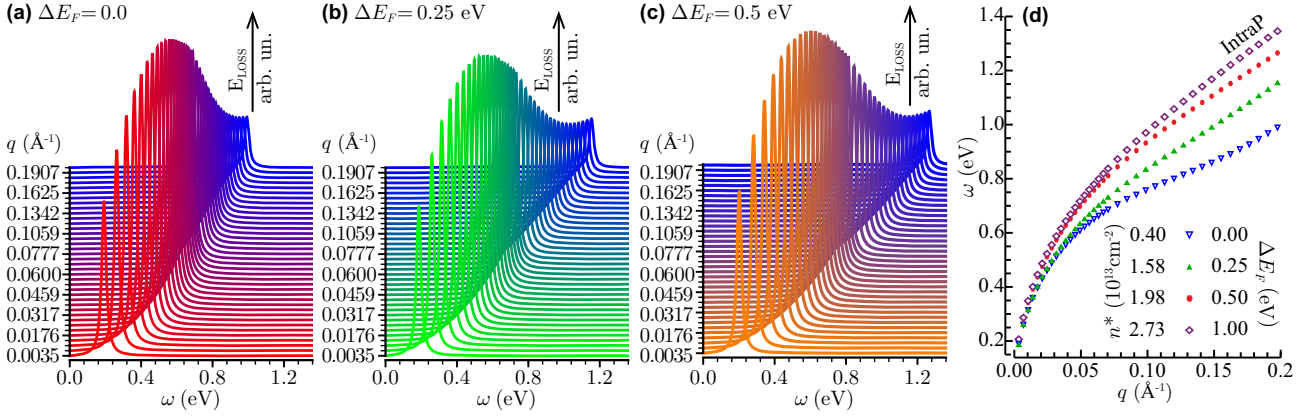


Figure S3. E_{LOSS} vs $\omega < 1.5$ eV for intrinsic and extrinsic 4ZGNR at $T = 300$ K. Fermi level shifts $\Delta E_F \leq 1$ eV, i.e., conduction-electron concentrations $n^* < 3 \times 10^{13}$ cm^{-2} , are considered. The EL spectra corresponds to some of the sampled momenta below 0.2 \AA^{-1} parallel to the GNR axis, and are shifted vertically for clarity.

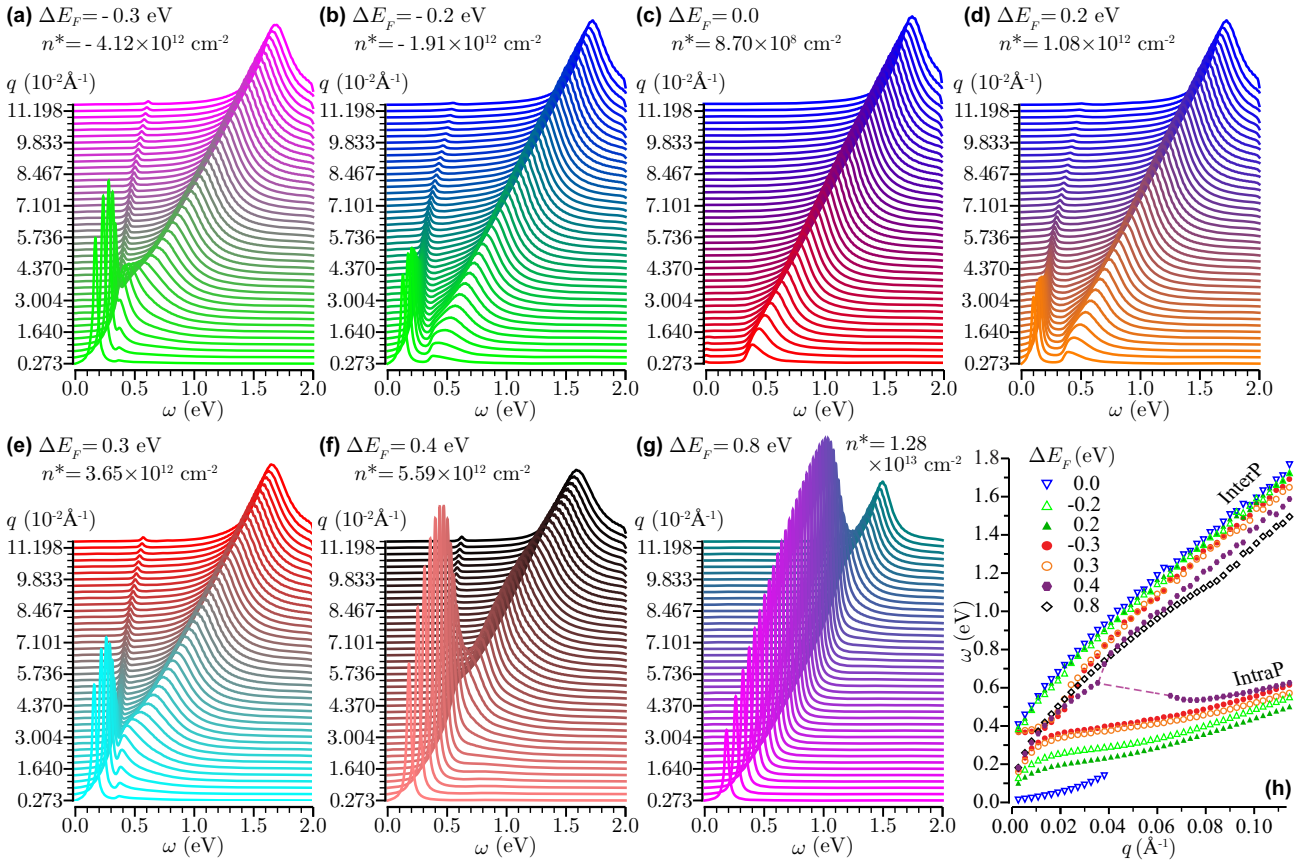


Figure S4. E_{LOSS} vs $\omega \leq 2$ eV for intrinsic and extrinsic 5AGNR at $T = 300$ K (a-g). Values of ΔE_F ranging from -0.3 to 0.8 eV are considered, which correspond to charge-carrier concentrations n^* of the order of $\pm 10^{12}$ cm^{-2} . The EL spectra corresponds to some of the sampled momenta below 0.15 \AA^{-1} along the GNR axis, and are shifted vertically for clarity. (h) (q, ω) dispersions for the intraband and interband plasmons in 5AGNR at $T = 300$ K (see also Fig.5(a))

These other features are highlighted in Fig. 5(a) and S4(h), where the intraband and interband plasmon dispersions of Fig. S4(a-g) are plotted together vs q and ω . Some of them are also separately visible in Fig. 4(a-d). Notice that a tiny intraband contribution should be present in undoped 5AGNR because of the

Fermi-Dirac population of low lying conduction states at room temperature. Indeed, 5AGNR is characterized by a conduction-electron concentration of $\sim 10^9$ cm^{-2} at $T = 300$ K, which is negligibly small with respect to that of 4ZGNR and MG. Nonetheless, local maxima in E_{LOSS} are recorded for $q < 0.04 \text{ \AA}^{-1}$, yielding the (ω, q)

dispersion in Fig. S4(h).

Also detectable in Fig. 5(a) and Fig. S4(h) is the effect of the slight asymmetry in the VB and CB of 5AGNR close to band gap (inset in Fig. 1(d)), which appears to influence the plasmon structure especially in the intraband components. This is due to the different charge-carriers concentrations originated from positive and negative doping values. Thus, the intraband plasmon of 5AGNR depends of the doping type (sign) even at frequencies of the order of ~ 50 THz.

The role of positive doping is also spotted in Fig. S5(a), where a comparison of the intraband plasmon dispersion of 5AGNR is attempted with the calculations of Ref. 24. The latter were based on a tight-binding (TB) gapless two-band model at the absolute zero. A two-dimensional Coulomb potential was adopted, depending on a localization parameter TBpz-w of the p_z orbitals. The correlation matrix elements (S4) were approximated by the low- q limit form $\langle \nu \mathbf{k} | \nu' \mathbf{k} + \mathbf{q} \rangle$. Of course, the detailed properties of the plasmon modes are critically dependent on the VB and CB dispersions, which are significantly different in DFT-LDA and TB calculations. The TB electronic features of 5AGNR allow only for intraband modes that, nevertheless, appear at the same scale as the TDDFT intraband plasmons of doped 5AGNR.

To have a closer look at the THz region, we performed TDDFT calculations on an MP mesh of $12500 \times 1 \times 1$ points, including only the contributions of VB and CB

states of 5AGNR in Eq. (1). Well converged results were obtained with a broadening lifetime parameter η of ~ 0.5 THz. The EL spectra for 5AGNR at $T = 300$ K and $\omega < 25$ THz are shown in Fig. S5(b). The plasmon dispersion curves are reported in Fig. S5(c) and compared to the semiclassical approach of Ref. 23, where plasmon resonances in doped GNR arrays of $10 - 100$ nm width were described by the following analytical expression:

$$\omega_p = \text{Re}(\sqrt{2\pi n^* q \cos^2 \theta / m^* - \eta^2} - i\eta) \quad (\text{S9})$$

Eq. (S9) (here given in Hartree au) depends on the concentration n^* of conduction electrons, whose effective mass m^* is directly proportional to the band gap E_{GAP} through the characteristic velocity $v_0 \sim 10^6$ m/s, i.e., $E_{\text{GAP}} = 2m^*v_0$. The transferred momentum is parametrized in terms of its in-plane modulus q and angle θ relative to the GNR axis. In our applications to 5AGNR, we considered only transferred momenta parallel to the GNR axis ($\theta = 0$). To use Eq. (S9), we estimated $m^* \sim 0.36$ corresponding to $E_{\text{GAP}} \sim 0.4$ eV and considered concentration values equivalent to the Fermi energy shifts $\Delta E_F = 0.2, 0.3, 0.4$ eV at $T = 300$ K. The analytical and numerical curves turned out to be amazingly similar for $\Delta E_F < 0.5$ eV. We may then infer that our TDDFT calculations on a narrow-size GNR show some consistency with predictions on larger GNR structures currently available for experiments.

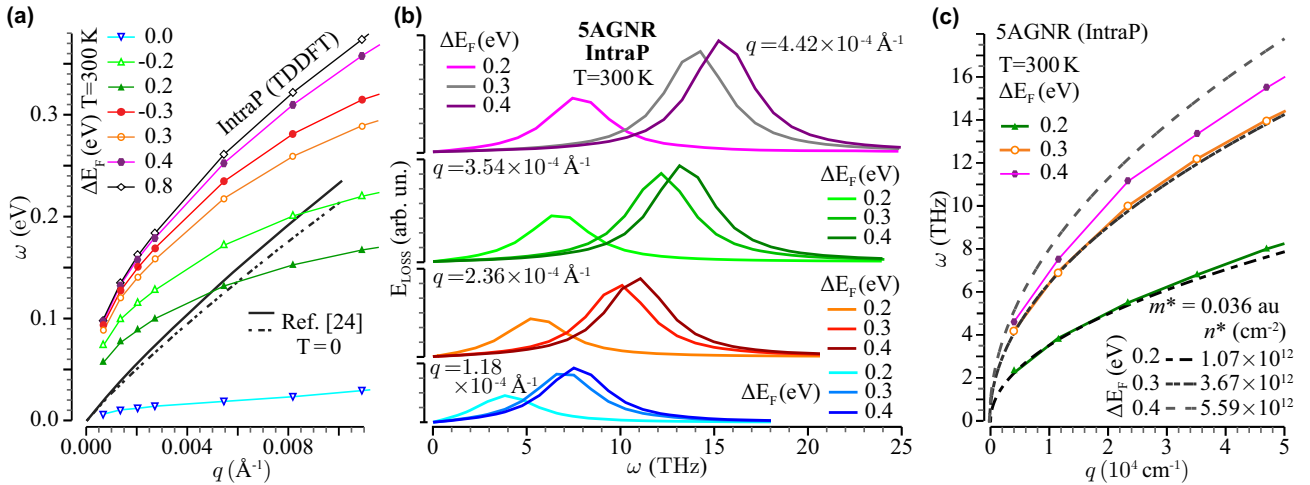


Figure S5. Intraband plasmon dispersions (a,c) and EL spectra (b) for 5AGNR at room temperature, low frequencies in the lower THz domain, and small transferred momenta. In (a) TDDFT calculations with the same settings as Fig. S4 are compared with the TB calculations of Ref. 24 (black continuous and dashed lines), where two different localization parameters were chosen to model the electron-electron interaction entering Eq. (S5); In (b) the EL spectra are computed with a TDDFT approach that include only the VB and CB states. In (c) the intraband plasmon dispersions of (b) are compared with the semiclassical model of Ref. 23

IV. TEMPERATURE EFFECTS IN SEMICONDUCTING GNRS

As shown in the main text and in the previous section, the large tunability in the intraband plasmon mode of

5AGNR is critically dependent on the electron (hole) occupancy of CB (VB) states, lying within an energy window of $0.5 - 1$ eV around the Fermi level. Such a population is given by the Fermi-Dirac statistical factors $f_{\nu \mathbf{k}}$ and $f_{\nu \mathbf{k} + \mathbf{q}}$ in Eq. (1) that are significantly influenced, within

the considered energy range, by even moderate temperature changes below ~ 1000 K. This effect inevitably plays a major role in any nanodevice design approach.

To quantify and characterize it, we ran EL calculations on undoped 5AGNR with electronic temperature values larger than 500 K.

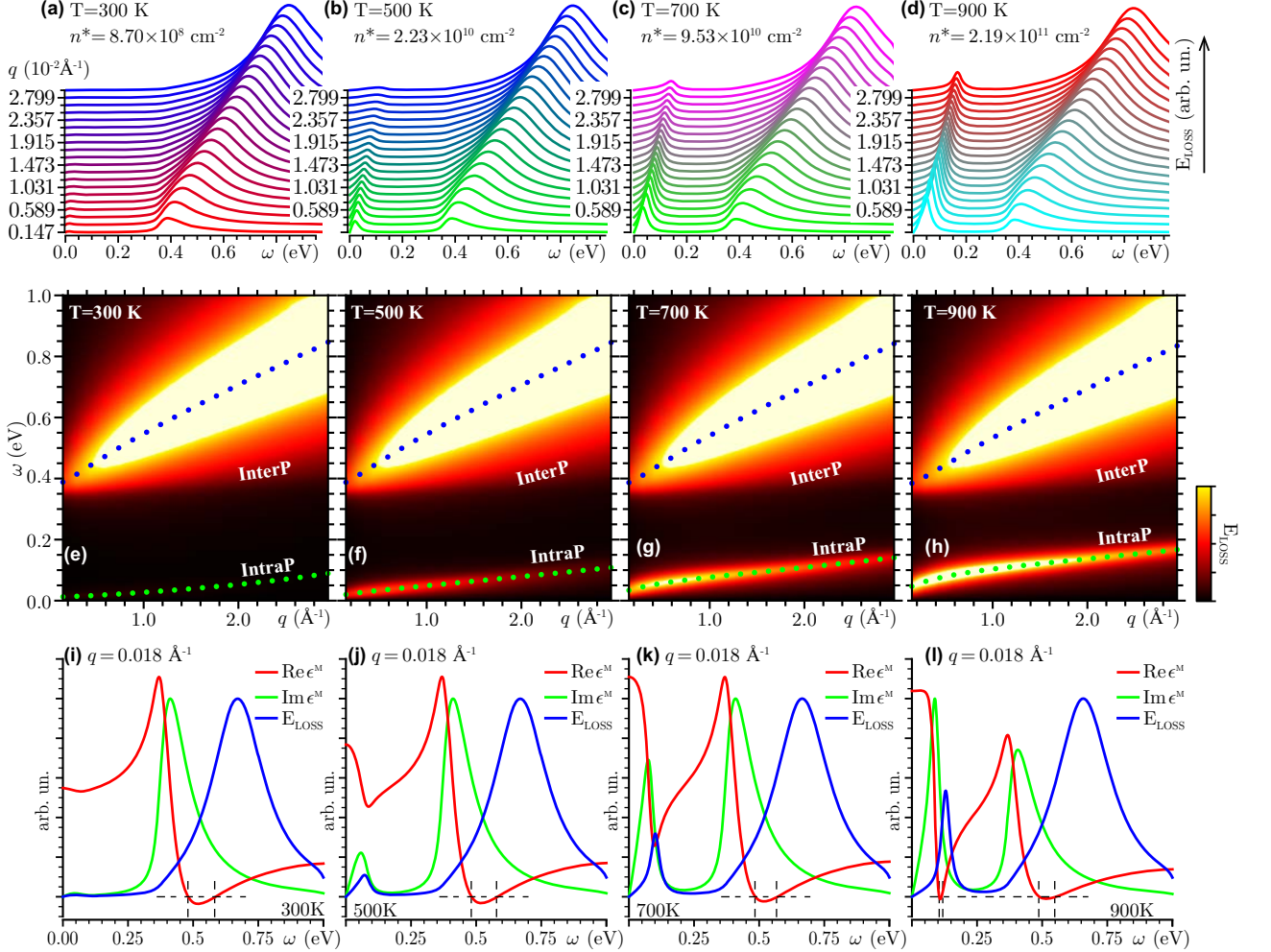


Figure S6. Dielectric response of intrinsic 5AGNR at $T = 300$ K (a,c,e), $T = 500$ K (b,d,f), $T = 700$ K (c,g,k), $T = 900$ K (d,h,i). E_{LOSS} is represented as sequence of shifted spectra in (a-d) and density plots in (e-h) with the same intensity scale as in Figs. 2, 3(a-d) and 4(a-d). The blue and green dots denote the intraband and interband plasmon (q, ω)-dispersions, respectively. $\text{Re}(\epsilon^M)$, $\text{Im}(\epsilon^M)$ and E_{LOSS} in In (i-l) are normalized as in Fig. 3(e-h) and 4(e-h). The dashed gridlines indicate the zeroes of $\text{Re}(\epsilon^M)$.

All other settings were the same as for room temperature calculations. The resulting EL spectra are reported in Fig. S6 for energies below ~ 1 eV and momentum transfers smaller than 0.03 \AA^{-1} .

At $T = 300$ K (Fig. S6(a)), the interband plasmon is clearly visible. Nevertheless a faint intraband peak may be spotted at energies below ~ 0.1 eV, and the intraband plasmon dispersion can be computed. As the temperature is increased to 500 K (Fig. S6(b)), the intraband plasmon peak begins to appear in the same intensity scale as the interband plasmon. At higher temperatures, say, $T = 700, 900$ K (Fig. S6 (c,d)), the intraband plasmon is well resolved and also well separated from the interband plasmon.

The increase of the intraband plasmon intensity is readily understood considering how the electronic temperature affects the population of the KS states near the Fermi level. At room temperature the number of electrons that are capable to overcome the 0.36 eV gap is small, with a concentration of the order of 10^9 cm^{-2} . Thus, interband excitations are dominant. At $T = 500$ K the electron population of the conduction band becomes appreciable, with a concentration of roughly $2 \times 10^{10} \text{ cm}^{-2}$, generating the small peak in the EL spectrum. As the Temperature further increases ($T \geq 700$ K), the smearing width of the Fermi-Dirac distribution function increases, the conduction electron concentrations become larger than 10^{11} cm^{-2} , and the intraband plasmon fully

appears in the EL spectrum. Charge carrier concentrations triggered by temperature increase are nevertheless much smaller than those obtained with doping or gating. For this reason, no particular interference is recorded in Fig. S6 between intraband and interband plasmon modes.

V. FINAL REMARKS

We have verified that ZGNRs and AGNRs offer the typical high-energy (>3 eV) interband excitations of carbon based materials^{34,40-43}, even though the energy of these excitations critically depends on the GNR width and in-plane distance between the GNRs. At lower energies (<1.5 eV), we have detected one intraband plasmon mode for the (semi)metallic ZGNR. In the same energy range, we have identified and characterized two modes in the semiconducting AGNR, i.e., one interband and one

intraband plasmons. The latter shows a large sensitivity to doping level as well as electronic temperature. The interplay between the two collective excitations in AGNR, which co-exist and interact with each other, represent the main result of our study. We have checked that intraband and interband plasmons appear also in larger AGNRs (not reported here). These findings require confirmation by measurements available on larger GNRs²², although the experiments of Ref. 17 seem to suggest that interband and intraband plasmon in low-gap GNRs exist, can be controlled and exploited for future nanodevice technology.

ADDITIONAL REFERENCES

⁴⁵ Broyden, C. G.; *IMA J. Appl. Math.* **1970**, *6*, 76.

⁴⁶ Fletcher, R.; *Comput. J.* **1970**, *13*, 317.

⁴⁷ Goldfarb, D.; *Math. Comp.* **1970**, *24*, 23.

⁴⁸ Shanno, D. F.; *Math. Comp.* **1970**, *24*, 647.